SI Appendix

Supplementary Methods

Intracranial recordings

Patients were implanted with intracranial electrodes for ~7 days with continuous recordings for seizure onset localization. Stereoelectroencephalography (SEEG) electrode implantation and targeting were made for purely clinical purposes. SEEG recordings were collected with a Nihon Kohden JE-120 amplifier at 1000 Hz sampling (patients S1-17), Natus Quantum LTM amplifier at 1024 Hz (patients S18-19), or Natus Xltek EMU128FS at 1000 Hz (patients S20-22). Standard clinical electrodes were 0.8 mm diameter, with 10-16 2 mm long contacts at 3.5-5 mm pitch (~150 contacts/patient). In addition, patients S19 and S22 had electrodes with 0.5-2 mm long contacts at 1-2 mm pitch.

Data were also collected from an intracranial microelectrode (Utah Array) implanted into cortical tissue that was suspected based on presurgical evaluation to be included within the region of the therapeutic resection. The Utah Array is a 10x10 microelectrode array with 400 μm contact pitch and corners omitted (1-3). The insulated probe lengths are 1 or 1.5 mm long with a base of 35-75 μm tapering to uninsulated platinum 3-5 μm tip. Data were acquired at 30 kHz sampling rate with a 0.3-7.5 kHz bandpass (Blackrock Microsystems), referenced with respect to a distant wire. The implantation of the array did not affect clinical monitoring. In all patients, the tissue into which the array was implanted was later resected to gain access to the surgical focus beneath, the electrode was determined not to be implanted in epileptogenic tissue, and seizures were determined not to originate from the area where the array was implanted.

During recordings the patients were reclining in their beds in the Epilepsy Monitoring Unit. During waking, typical activities were reading, thinking, looking out the window, watching TV or videos, and speaking with family, friends, or hospital personnel. These distractions were prevented while performing the memory task. We rejected periods where the recordings displayed movement artifacts, epileptiform activity, or increased slow activity which may suggest drowsiness.

Electrophysiology pre-processing

Offline data preprocessing was performed in MATLAB 2019b and local field potentials (LFPs) were inspected visually using the FieldTrip toolbox (4). SEEG data were downsampled to 1000 Hz with anti-aliasing and 60 Hz notch filtered (zero-phase) with 60 Hz harmonics up to 480 Hz. Transcortical contact pairs were identified using both anatomical location (using the pre-operative MRI aligned to the post-operative CT), and physiological properties (high amplitude, coherence, and inversion of spontaneous activity between contacts), and selected such that no 2 pairs shared a contact, with the exception of the 1 mm spaced hippocampal bipolar channels described above. All SEEG analyses were performed using bipolar derivations between contacts separated by 1-5 mm in cortical or hippocampal gray matter in order to ensure that activity was locally generated (5). All bandpasses, lowpasses, and highpasses were performed by applying a 3^{rd} order butterworth filter (MATLAB: *butter*) in the forward and reverse directions (MATLAB: *filtfilt;* 6^{th} order total; zero-phase shift).

Channel selection

Channels were excluded from analysis if they were in lesioned tissue, involved in the early stages of the seizure discharge, had frequent interictal activity, or abnormal LFPs. From the total 2772 bipolar channels (1326 left hemisphere) in the 22 SEEG patients (S1-22), 52 hippocampal (24 left hemisphere) and 403 transcortical (180 left hemisphere) bipolar channels were selected for the analyses (Supplementary Table 1). Polarity was corrected for individual bipolar channels such that downstates were negative and upstates were positive. This was accomplished by ensuring that during non-rapid eye movement sleep (NREM), negative peaks were associated with decreased, and positive peaks were associated with increased, mean ±100 ms 70-190 Hz analytic amplitude, an index of cell firing that is strongly modulated by downstates and upstates (6).

Electrode localization

Cortical surfaces were reconstructed from the pre-operative whole-head T1-weighted structural MR volume using the standard FreeSurfer recon-all pipeline (7). Atlas-based automated parcellation (8) was used to assign anatomical labels to regions of the cortical surface in the Destrieux atlas (9). In addition, automated segmentation was used to assign anatomical labels to each voxel of the MR volume, including identifying voxels containing hippocampal subfields (10). In order to localize the SEEG contacts, the post-implant CT volume was registered to the MR volume, in standardized 1 mm isotropic FreeSurfer space, using the general registration module (11) in 3D Slicer (12). The position of each SEEG contact, in FreeSurfer coordinates, was then determined by manually annotating the centroids of electrode contacts visualized in the co-registered CT volume. Each transcortical contact pair was assigned an anatomical parcel from the atlas above by ascertaining the parcel identities of the surface vertex closest to the contact-pair midpoint. Subcortical contacts were assigned an anatomical label corresponding to the plurality of voxel segmentation labels within a 2-voxel radius. Transcortical contact pair locations were registered to the fsaverage template brain for visualization by spherical morphing (13). White-matter streamline distances between channels computed using the 360 parcels of the HCP-MMP1.0 atlas (14), as determined by probabilistic diffusion MRI tractography (15), are population averages from Rosen and Halgren (2021) (16). When two channels were in the same HCP parcel the fiber tract distance was defined as 0.

Sleep and waking epoch selection

Epochs included in the study did not fall within at least 1 hour of a seizure and were not contaminated with frequent interictal spikes or artifacts. NREM periods were selected from continuous overnight recordings where the delta (0.5-2 Hz) analytic amplitude from the cortical channels was persistently increased (Supplementary Table 1). Sleep epochs were confirmed by visual inspection to have normal appearing spindles, downstates, and upstates. Waking periods were selected from continuous daytime recordings that had persistently low cortical delta as well as high cortical alpha (8-12 Hz), beta (20-40 Hz), and high gamma (70-190 Hz) analytic amplitudes. When the data included electrooculography (EOG; *N*=15/17 SEEG patients S1-17), waking periods also required that the 0.5-40 Hz analytic amplitude of the EOG trace was increased. Waking epochs were required to be separated from periods of increased delta analytic amplitude by at least 30 minutes.

Paired-associates memory task

Paired-associates memory task data were collected from 5 patients using Presentation (Neurobehavioral Systems). Patients were instructed to memorize a series of word pairs and to

recall the second word when cued with the first. A word pair was presented with text and audio (pre-recorded speech) along with an integrating image that contained semantic content of both words. After each presentation, immediate recall was assessed by cuing the first word immediately after the offset of the word pair and image. The patient then attempted to recall the word aloud. This was repeated with 8 different pairs followed by a 6 s break, and then delayed recall of the 8 pairs was assessed in the same order where the first word was cued and the patient attempted to recall the second word aloud. After 4 s the integrating image was displayed. Delayed recall was only considered successful if the second word was said aloud before the image appeared. This sequence was repeated 20 times for a total of 160 word pairs. For one patient (S18), the task was instead structured as 25 sets of 6 pairs with the integrating image shown during the encoding period but not during delayed recall, and instead during delayed recall the second word was presented after 5 s. Delayed recall was only considered successful for this patient if the second word was said aloud before it was presented after 5 s. Task performance by patient is summarized in Supplementary Table 5.

During the task, audio containing the stimulus presentations and patient voice was split and simultaneously recorded into the task presentation computer and into the clinical amplifier system synchronously with the intracranial recordings. Stimulus markers sent by the task computer were also synchronized with the intracranial recordings. Scoring of behavioral data was done offline by listening, and recall onsets were identified offline using Audacity v2.4.2 through both visual examination of the task computer recorded audio waveforms and spectrograms as well as confirmation through listening. The computer recorded audio was downsampled with anti-aliasing to 1000 Hz and cross-correlated with the audio recorded alongside the intracranial recordings to ensure high temporal precision of recall onsets.

Ripple occurrences and co-occurrences relative to the word cue (text and audio) preceding recall onsets prior to successful (i.e., correct response before the answer or integrating image was presented in the delayed condition) or unsuccessful (i.e., no response, incorrect response, or response after the answer or image was presented) were computed across trials, where each trial was an average across channels. Null distributions of occurrences were computed by randomly shuffling ripple or co-occurring ripple centers for each channel in each trial within ±3 s from cue onset 10 times. Observed over chance (average of null) ripple occurrence and co-occurrence histograms had 25 ms bins Gaussian-smoothed with a 100 ms window (σ=20 ms). Trial-wise ripple occurrence and co-occurrence averages in the 150-300 ms window following cue onset were computed for statistical analyses.

Sleep spindle detection

Spindles were detected as previously described (17). Data were bandpassed at 10-16 Hz, then absolute values were smoothed via convolution with a tapered 300 ms Tukey window. Next, median values were subtracted from each channel. Data were normalized by the median absolute deviation and spindles were detected when peaks exceeded 1 for at minimum 400 ms. Onsets and offsets were identified when these amplitudes fell below 1. Putative spindles that coincided with large increases in lower (4-8 Hz) or higher (18-25 Hz) frequency power were rejected to eliminate broadband events (e.g., artifacts) as well as theta bursts, which may extend into the lower end of the spindle range (18).

Sharpwave-ripple and spindle-ripple detection

Additional analyses were performed specifically on sharpwave-ripples and spindle-ripples detected according to our previous methods (19, 20). First, NREM data were bandpassed from

70-100 Hz, and a putative ripple was detected when the 20 ms moving root-mean-squared amplitude exceeded the 90th percentile. Ripples were required to have at least 3 distinct oscillation cycles as described above. Broadband LFP data ±2s around ripple centers underwent 1-D wavelet (Haar and Daubechies) decomposition to detect and remove sharp transients. Ripples were classified as sharpwave-ripples based on the similarity of the peri-ripple LFP to the 400 ms average biphasic waveform template created for each patient using 100-300 hand-marked hippocampal sharpwave-ripples, as quantified by the dot product between the template and the peri-ripple LFP (-100 to 300 ms), and the absolute difference between the LFP value at the ripple center. Ripples were classified as spindle-ripples if the ripple center occurred during a hippocampal spindle, detected in the same way as described in the Supplementary Information for cortical spindles, on the same channel. Ripples could be classified as both sharpwave-ripples and spindle-ripples if they met both of these criteria.

Interictal spike detection and rejection

Ripples and sleep graphoelements were excluded if they were within ±500 ms from a putative inter-ictal spike (IIS) detected as follows. A high frequency score was computed by smoothing the 70-190 Hz analytic amplitude with a 20 ms boxcar function and a spike template score was generated by computing the cross-covariance with a template interictal spike. The high frequency score was weighted by 13 and the spike score was weighted by 25, and an IIS was detected when these weighted sums exceeded 130. In each patient, detected IIS and intervening epochs were visually examined from hippocampal and cortical channels (when present) to confirm high detection sensitivity and specificity.

Time-frequency analyses

Average time-frequency plots of the ripple event-related spectral power (ERSP) were generated from the broadband LFP using EEGLAB (21). ERSP was calculated from 1 Hz to 500 Hz with 1 Hz resolution with ripple centers at t=0 by computing and averaging fast Fourier transforms with Hanning window tapering. Each 1 Hz bin of the time-frequency matrix was normalized with respect to the mean power at -2000 to -1500 ms and masked with two-tailed bootstrapped significance (N=200) with false discovery rate (FDR) correction and α=0.05 using -2000 to -1500 ms as baseline.

Ripple phase lag analyses

The phase lag between co-occurring cortical ripples (25 ms minimum overlap) was computed for channels with significant PLV modulations (see above) by finding the circular mean (22) of the angular difference between the two 70-100 Hz bandpassed ripples during their overlapping period during each ripple that co-occurred between the two channels. The mean phase lag for a given channel pair was computed by finding the circular mean of these circular means. For each channel pair that had a significant PLV modulation, differences in ripple phase lags by sleep night were computed for each sleep night pair where both nights had at least 30 co-ripples using the Watson-Williams multi-sample test for equal means.

Unit detection, classification, quality, and isolation

Unit detection and classification was performed according to our published procedures (23-29). Data were bandpassed at 300-3000 Hz and putative unit spikes were detected when the filtered signal exceeded 5 times the estimated standard deviation of the background noise. Units were k-means clustered using the first three principal components of each spike. Overlaid spikes were

examined visually and those with abnormal waveforms were excluded. Based on their waveforms, firing rates, and autocorrelograms, action potentials were clustered as arising from putative pyramidal cells or interneurons. Putative pyramidal cells had spike rates of ~0.1-0.8 Hz, long valley-to-peak and half width intervals, sharp autocorrelations, and bimodal inter-spike interval (ISI) distributions, reflecting a propensity to fire in bursts (Supplementary Table 7). By contrast, putative interneurons had spike rates of ~1-5 Hz, short valley-to-peak and half width intervals, broad autocorrelations, and a predominantly unimodal ISI distribution.

Single unit quality and isolation were confirmed according to previously established guidelines (30). Unit spikes were verified to well-exceed the noise floor based on large peak signal-to-noise ratios (PY: 9.12±3.39; IN: 5.23±2.88). Since the neuronal spiking refractory period is about 3 ms, the percent of ISIs less than 3 ms estimates the degree of single unit contamination by spikes from different units, which was very low among the units included in this study (PY: 0.21±0.34%; IN: 0.33±0.58%). Furthermore, single units detected on the same contact were highly separable according to their projection distances (31) (PY: 95.4±86.0 SD; IN: 82.8±83.4 SD). Lastly, temporal stability of unit spikes over time was confirmed based on consistency of the mean waveform shape and amplitude of each unit across recording quartiles.

Removal of unit spikes from local field potentials

When detecting high frequency oscillations in an LFP from a microelectrode capable of detecting unit spikes, these unit spikes may contaminate the LFP (32), leading to false positive ripple detections. Notably, lowpassing and downsampling does not eliminate the effect of the action potential on the LFP. Therefore, we implemented a modified unit spike template subtraction technique (33). Specifically, the average unit spike waveform (-500 μs to 1600 μs centered on the trough) of each unit was subtracted from the same channel's unfiltered 30 kHz Utah Array data, centered on each spike. These data were then downsampled to 1 kHz and the detection of ripples was performed as described above. Extensive visual confirmation of events in the 30 kHz LFPs confirmed that this method resulted in the detection of true oscillations.

Analyses of unit spiking during ripples

Unit spiking was analyzed with respect to local ripples detected on the same contact. Ripple phases of unit spikes were determined by finding the angle of the Hilbert transform of the 70-100 Hz bandpassed signal (zero-phase shift) at the times of the spikes. Unit spiking modulations during ripples were computed by comparing the number of spikes for each unit during ripples divided by the number during non-ripple epochs, i.e., epochs in between ripples, that were matched in number and duration to the ripples.

Statistical analyses

All statistical tests were evaluated with α=0.05. All *p*-values involving multiple comparisons were FDR-corrected according to Benjamini and Hochberg (1995) (34). FDR corrections across channel pairs were done across all channels pairs from all patients included in the analysis. Box-and-whisker plots show median, mean, and interquartile range, with whiskers indicating 1.5 × interquartile range, with outliers omitted. Significance of linear correlations were assessed using the significance of the correlation coefficient, *r*, when there were at least 10 data points.

In temporal analyses (i.e., peri-ripple time histograms), *p*-values were corrected across bins and all channels from all patients. To compute *p*-values using randomization tests, the observed test

statistic (e.g., events per bin) was compared to the null distribution of test statistics. Null distributions were randomly selected from the same epochs using 200 iterations. The *p*-value was computed as the proportion of null test statistics equal to or greater/less than the observed test statistic. Randomization tests were one-sided according to whether the observed test statistic was greater than or less than the mean of the null test statistics. Order preferences (e.g., of ripples between channels) were assessed using a two-sided binomial test with an expected probability of 0.5. To determine if a circular distribution was non-uniform, the Hodges-Ajne test was used. To determine if two circular distributions had different circular means, the Watson-Williams multi-sample test was used. To test if co-rippling between two particular cortical sites made it more likely that additional cortical sites co-rippled, we computed a χ^2 test of proportions for all possible groups of three cortical channels under the null hypothesis that the co-occurrence of channel A and B has no relation to the co-occurrence of A and C. Each table was made from the number of ripples in A that co-occurred with a ripple in B only, or C only, or both, or neither, where A occurring with B or not B are the 2 rows, and A occurring with C or not C are the 2 columns.

In the paired-associates memory analysis, chance ripple occurrences (or co-occurrences) were computed for each trial (thus separately for immediate and delayed recall) as the average of 200 random shuffles per channel (pair) within ±3 s from recall onset. Linear mixed-effects models were performed with the patient as the random effect, as follows:

$$\textit{(co-)ripples} \sim \textit{condition} + (1 \mid \textit{patient}) \quad (1)$$

Where *(co-)ripples* was the dependent variable computed as the average ripple rate (or co-ripple rate; minimum of 25 ms overlap for each co-ripple) within 150-300 ms following the stimulus cue preceding successful recall onset across trials, with the value for each trial as the average across channels, *condition* was 1) immediate recall or chance, 2) delayed recall or chance, 3) immediate recall or delayed recall (as a ratio of observed over chance), or 4) successful recall or unsuccessful recall (as a ratio of observed over chance). Chance levels were determined separately for immediate and delayed recall. Linear mixed-effects models with the same model formula as the one described above, with the patient as a random effect, were used to evaluate channel pair co-ripple metrics (co-occurrence probabilities, PLV modulations, and proportion of pairs with significant PLV modulations) with respect to fiber tract distance.

Differences in co-ripple phase lag preferences between nights was assessed using the Watson-Williams multi-sample test for equal means. To test if unit spiking increased during ripples, a two-sided two-sample *t*-test was used to compare the spike counts during ripples vs. the spike counts during baseline periods selected in between ripples, which were matched in number and duration to the ripples. Ripple phase-modulations of spiking for each unit with at least 30 spikes during local ripples was assessed by comparing counts within $0 \pm \pi/2$ vs. $\pi \pm \pi/2$, with an expected value of 0.5. This analysis was chosen in view of animal studies indicating that cell firing during ripples tends to have maximum contrast between these intervals.

Supplementary Figures

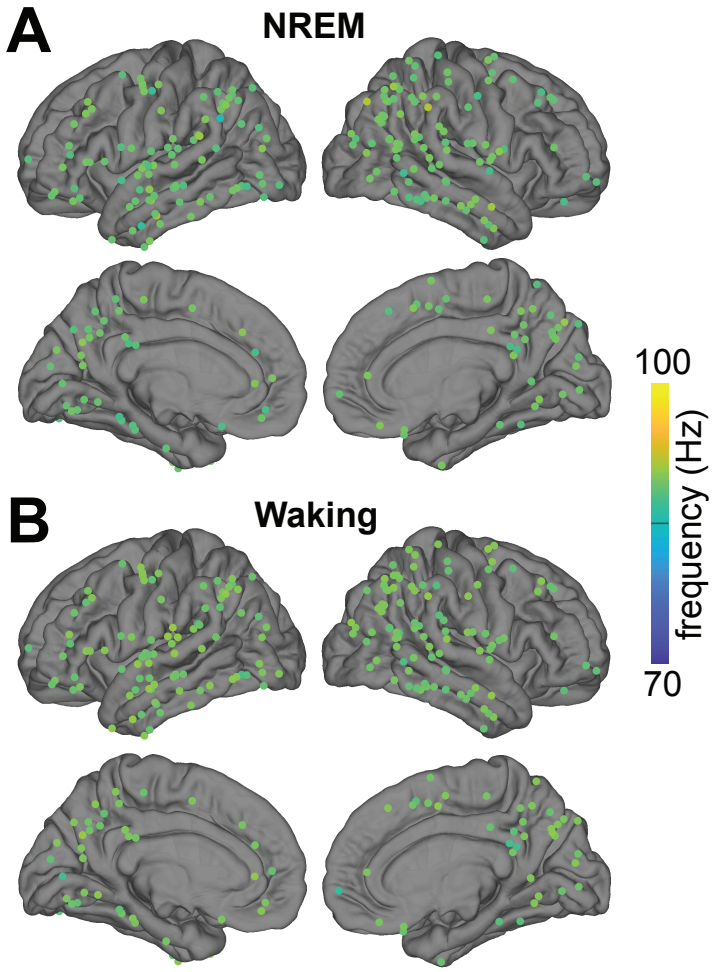

Supplementary Fig. 1. Cortical ripple frequencies across all channels from all patients. (**A**) Cortical ripple oscillation frequencies mapped across the cortex during NREM. Each marker depicts the average ripple frequency in a given channel (*N*=273 bipolar channels from SEEG patients S1-17). Color range spans the ripple band used for detection (70-100 Hz). (**B**) Same as (A) except for waking. Note the highly consistent frequency of ~90 Hz across lobes and between hemispheres during both NREM and waking. NREM=non-rapid eye movement sleep.

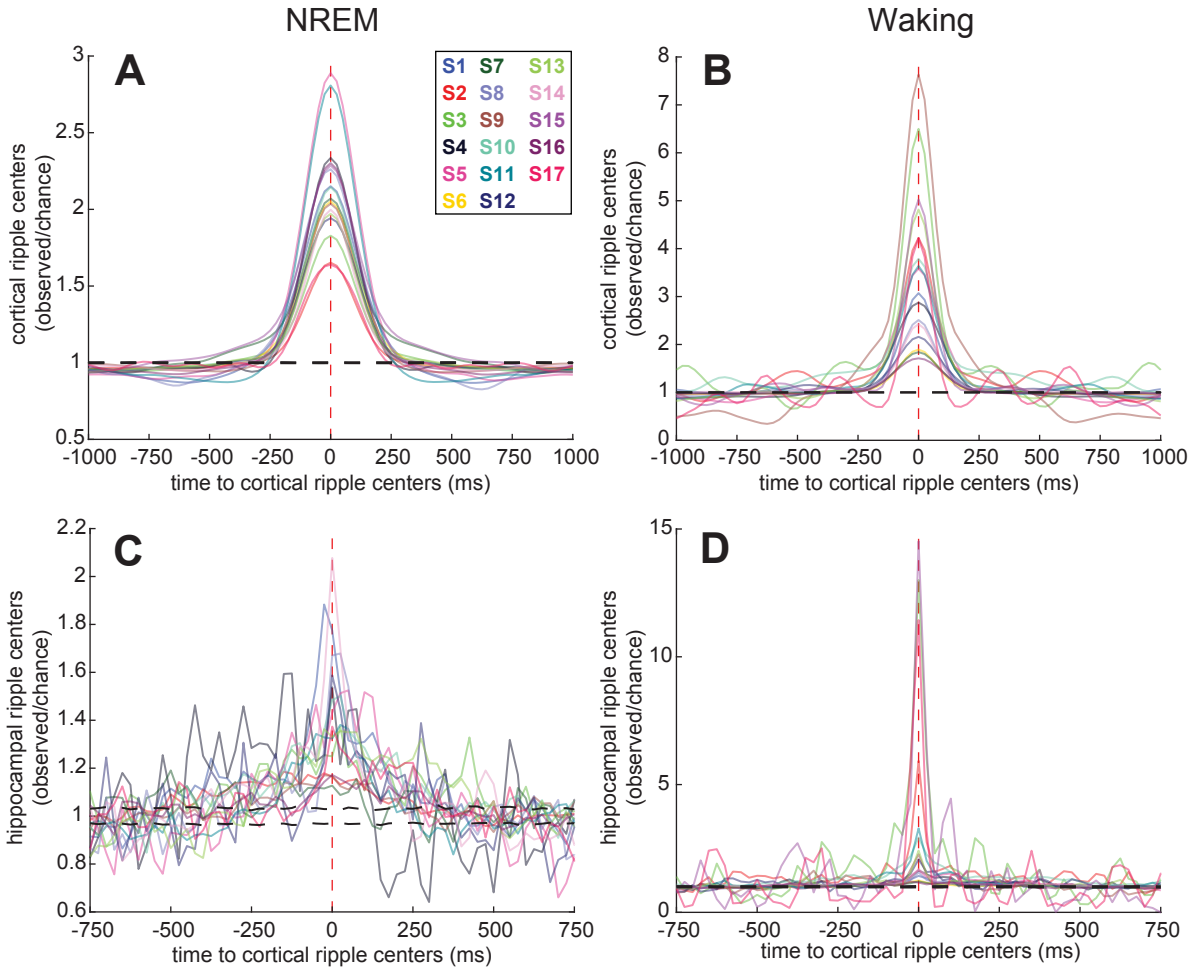

Supplementary Fig. 2 Cortico-cortical and hippocampo-cortical ripple coupling for individual patients. (**A-B**) Cross-correlograms of ripple times between all possible cortical sites in NREM (**A**) and waking (**B**) for individual patients (S1-17). Dashed black curves show 99% confidence interval of the null distribution (200 shuffles/channel pair). (**C-D**) Same as (A-B) except cross-correlograms of hippocampal ripple times relative to cortical ripple times. See Fig.2A-B for aggregate results.

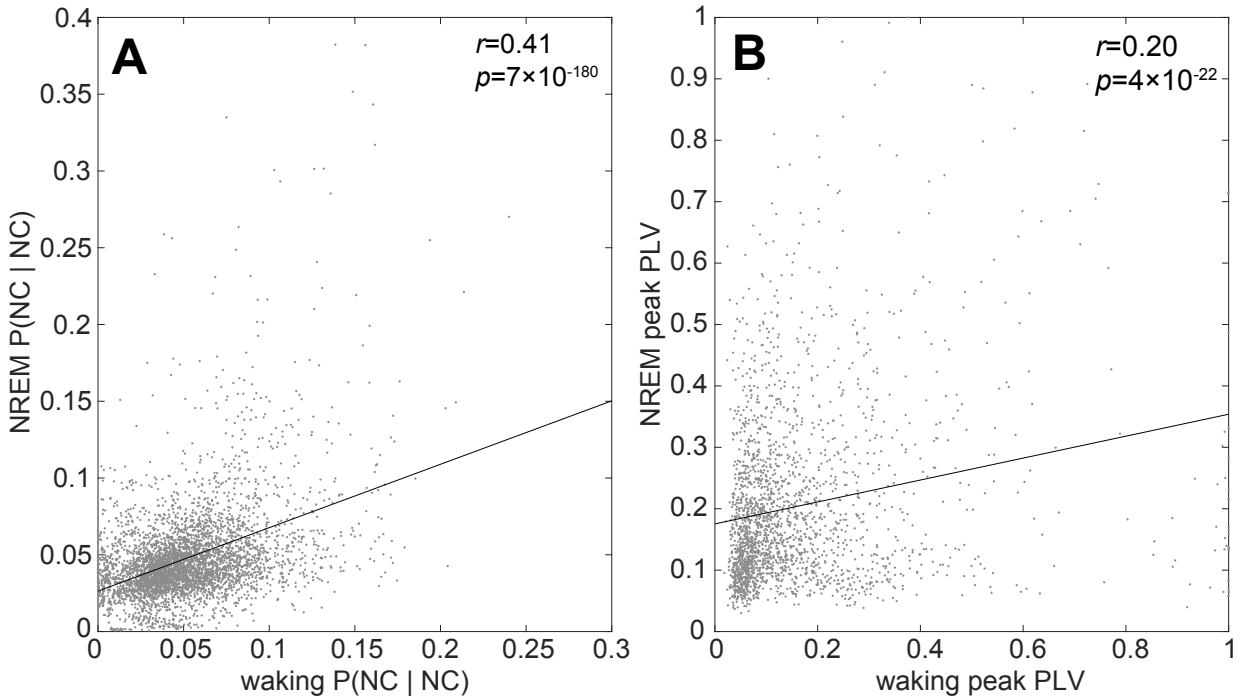

Supplementary Fig. 3. Cortico-cortical ripple co-occurrences and phase-locking are correlated between NREM and waking. (**A**) There was a significant correlation of the conditional co-occurrence probabilities of cortico-cortical ripples across channel pairs between NREM and waking (r=0.41, p=7×10^{-180}, significance of r). Each point represents a channel pair. (**B**) Same as (A) except for the peak PLV during co-occurring ripples for channel pairs that had significant PLV modulations (r=0.20, p=4×10^{-22}). NC=neocortex, PLV=phase-locking value.

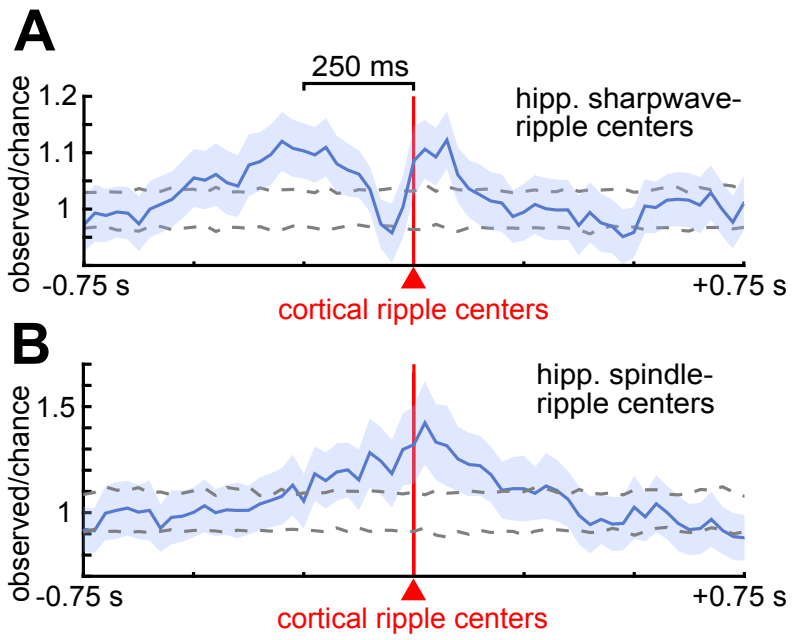

Supplementary Fig. 4. Hippocampal sharpwave-ripples precede and spindle-ripples coincide with cortical ripples. (**A-B**) Time delays from cortical ripples (*t*=0) to hippocampal sharpwave-ripples (**A**; *N*=91/461 significant channel pairs) and spindle-ripples (**B**; *N*=56/461) during NREM (post-FDR $p<0.05$, randomization test). Plots show average and SEM across significant channel pairs. Dashed curves show 99% confidence interval of the null distribution (200 shuffles/channel pair). FDR=false discovery rate correction, SEM=standard error of the mean.

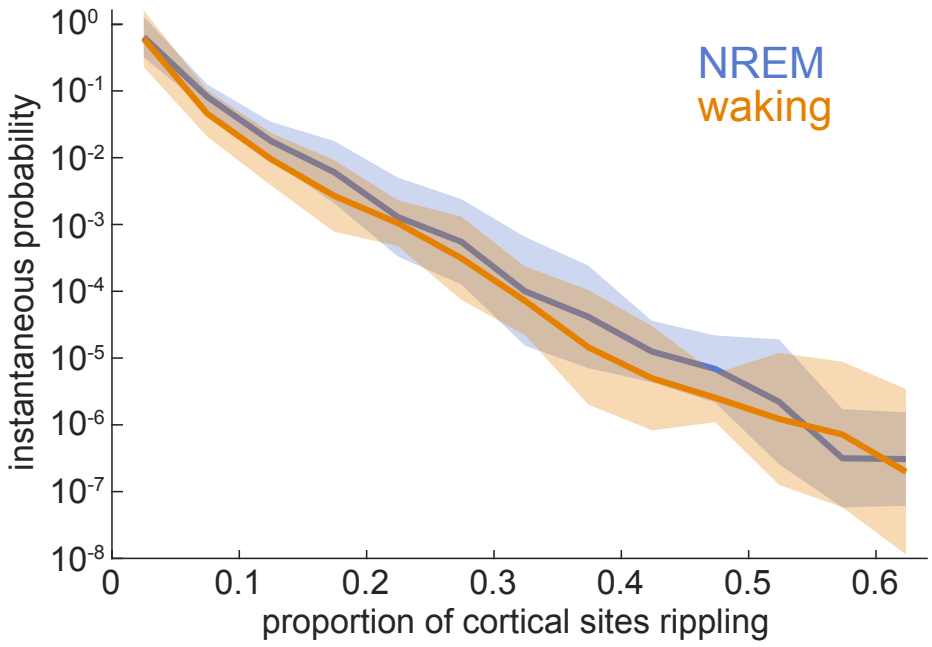

Supplementary Fig. 5. Instantaneous probabilities of the proportions of sites rippling together. Mean log-probability of the proportion of channels that is rippling at an arbitrary point in time during NREM or waking (*N*=273 channels from patients S1-17). Note that random co-rippling would be expected to be greater during NREM because of the greater ripple density, however, the instantaneous probabilities are similar between NREM and waking. Thus the similar curves shown here imply a relatively greater increase over chance during waking, as shown in Fig.2D. Data are binned in 0.05 increments. Error shows SEM.

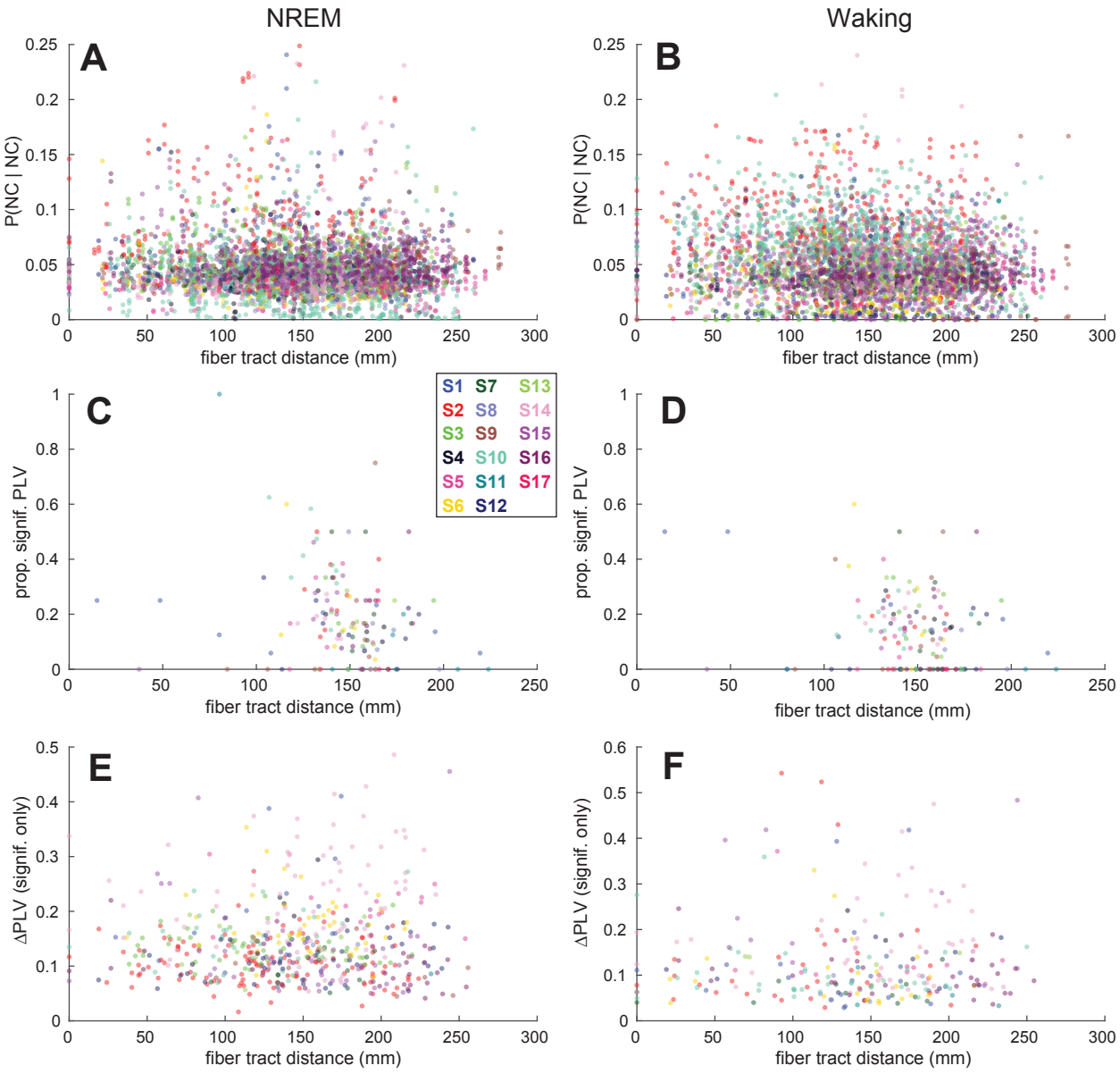

Supplementary Fig. 6. Cortico-cortical ripple co-occurrence and phase-locking across distance for individual patients. (**A-B**) Cortical ripple co-occurrence probabilities for each channel pair in NREM (**A**) and waking (**B**) over intervening fiber tract distance (16) for individual patients (S1-17). (**C-D**) Proportion of channel pairs with significant PLVs over distance in NREM (**C**) and waking (**D**) for individual patients. (**E-F**) ΔPLV over distance for channel pairs with significant co-ripple PLV modulations in NREM (**E**) and waking (**F**) for individual patients.

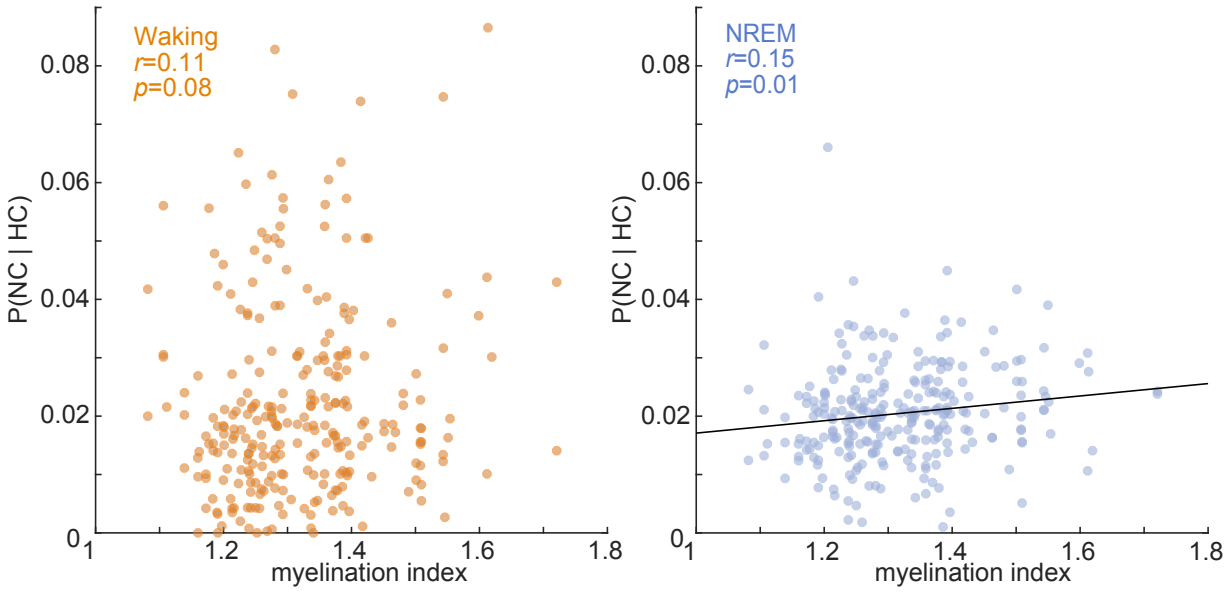

Supplementary Fig. 7. Hippocampo-cortical ripple co-occurrence as a function of cortical myelination index. Values are channel pair averages (each point is the average across pairs when there were multiple hippocampal channels in a patient) of the probability of a cortical ripple given a hippocampal ripple as a function of the cortical parcel myelination index (16). Co-occurrence required a minimum of 25 ms overlap.

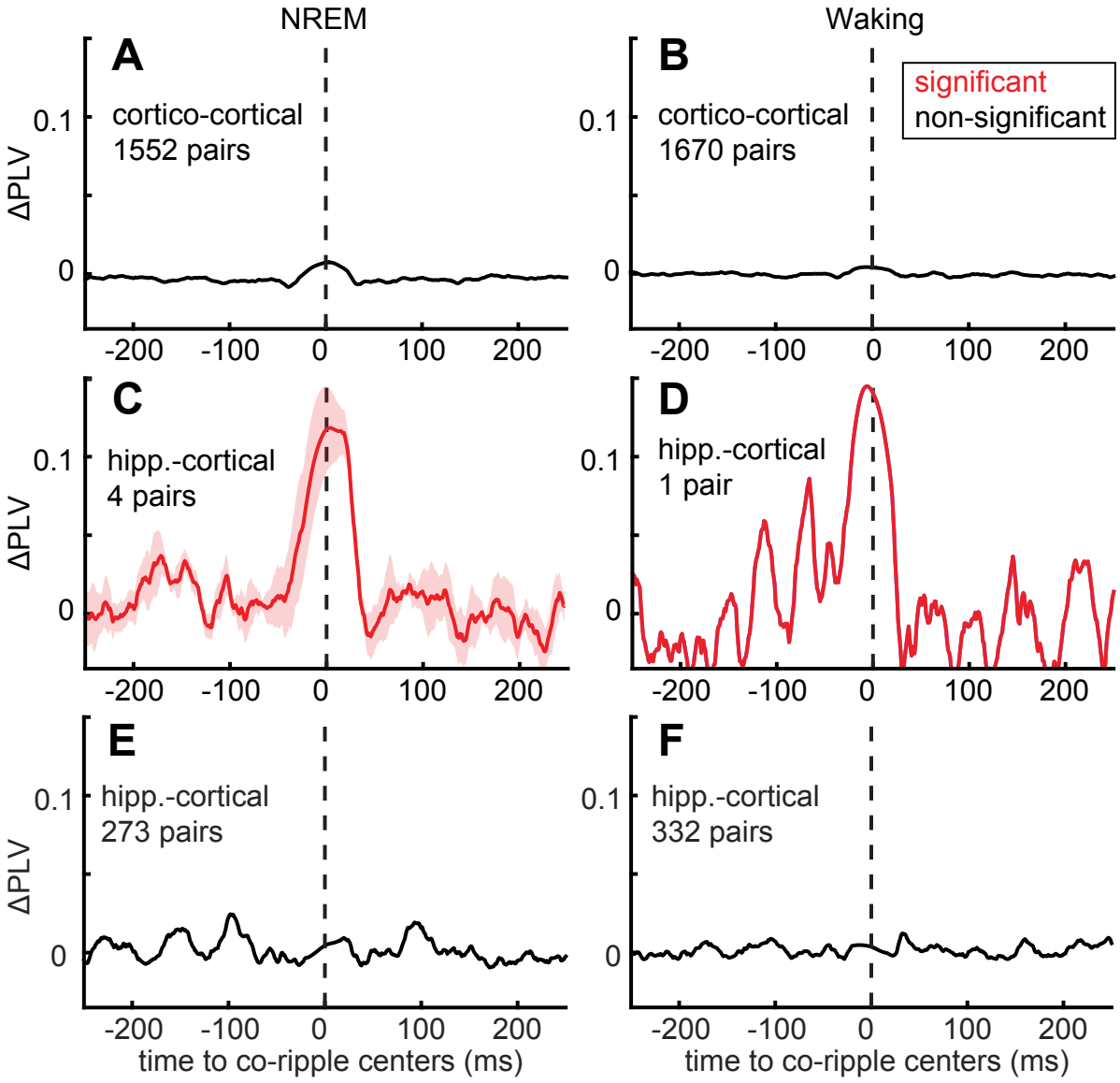

Supplementary Fig. 8. Non-significant cortico-cortical and significant and non-significant hippocampo-cortical co-ripple phase-locking results. (A-B) Average non-significant PLV time-courses locked to co-occurring ripples at *t*=0 for cortico-cortical pairs that had at least 40 co-occurring ripples during NREM (**A**) and waking (**B**). (**C-D)** Same as (A-B) except for hippocampo-cortical pairs with significant PLV modulations. All significant hippocampo-cortical channel pairs localized to hippocampus proper and cortex. (**E-F)** Same as (C-D) except for non-significant PLV time-courses. Shaded error shows SEM.

Supplementary Tables

Patient	Age	Sex	Hand.	No. Cort. Ch.	No. Hipp. Ch.	NREM Dur. (hr)	Waking Dur. (hr)	δ NREM / δ Waking	Paired-associates task
S1	20	M	R	18 (L)	1 (L)	6.1	49.8	3.98	-
S2	58	F	R	22 (L)	2 (L)	23.7	23.8	2.35	-
S3	42	M	L	16 (3 L)	3 (2 L)	11.4	19.3	3.39	-
S4	18	F	L	15 (R)	2 (R)	2.7	2.2	3.02	-
S5	20	F	R	18 (7 L)	2 (R)	5.6	19.3	2.93	-
S6	22	M	LR	17 (L)	1 (L)	6.3	59.9	5.45	-
S7	30	F	R	13 (2 L)	1 (R)	20.5	76.7	4.46	-
S8	43	F	R	12 (L)	2 (L)	8.1	32.6	5.43	-
S9	16	M	R	16 (4 L)	1 (R)	16.3	4.8	2.50	-
S10	32	F	R	29 (3 L)	3 (1 L)	11.2	27.6	3.11	-
S11	21	F	L	8 (4 L)	3 (2 L)	16.0	52.6	3.04	-
S12	21	F	R	14 (13 L)	1 (L)	26.2	37.2	2.92	-
S13	29	F	R	15 (6 L)	2 (1 L)	8.6	24.6	3.75	-
S14	41	F	R	18 (R)	1 (R)	11.9	63.3	4.20	-
S15	24	M	R	21 (9 L)	1 (L)	11.8	11.6	3.27	-
S16	31	F	R	15 (7 L)	1 (L)	28.1	39.4	2.55	-
S17	21	M	R	6 (L)	1 (L)	11.3	18.9	1.41	-
S18	25	M	R	38 (R)	0	N/A	N/A	N/A	✓
S19	32	M	L	21 (R)	8 (R)	N/A	N/A	N/A	✓
S20	34	M	R	22 (20 L)	0	N/A	N/A	N/A	✓
S21	38	F	R	21 (13 L)	0	N/A	N/A	N/A	✓
S22	23	M	R	28 (14 L)	16 (8 L)	N/A	N/A	N/A	✓

Supplementary Table 1. Stereoelectroencephalography patient demographics and data characteristics. Channels are the bipolar channels included in the analyses. δ NREM / δ Waking reports the ratio of the mean of the delta (0.5-2 Hz) analytic amplitude means across cortical channels during the NREM vs. waking epochs analyzed.

Ripple | Ripple	Significant Modulation	
	NREM	Waking
Cort-R | Cort-R	98.90% (3246/3282)	97.99% (3216/3282)
Hipp-R | Cort-R	26.78% (15/56)	64.28% (36/56)

Supplementary Table 2. Cortical ripple coupling with cortical or hippocampal ripples in interictal-free channels. While the coupling analyses presented in the main text were performed between non-epileptogenic sites, during periods that did not exhibit frequent interictal spikes or artifacts (35), and with ripples that were not contaminated with interictal spikes or artifacts, additional analyses were run on a subset of hippocampal (*N*=5 channels from patients S4, 6, 9, 17) and cortical channels (*N*=232 channels from patients S1-17) that did not have interictal spikes. These results demonstrate that cortico-cortical and hippocampo-cortical ripple coupling during both NREM and waking is present in the cases when both sites are free of interictal spikes. Numbers in parentheses are channel pair counts. *P*-values were FDR-corrected across channel pairs and bins.

	NREM			Waking		
Subject	Significant Modulation	Significant Sidedness	Cort-R Leading	Significant Modulation	Significant Sidedness	Cort-R Leading
S1	33.3% (6/18)	33.3% (2/6)	0% (0/2)	88.9% (16/18)	62.5% (10/16)	100.0% (10/10)
S2	77.3% (34/44)	50.0% (17/34)	5.9% (1/17)	100% (44/44)	11.4% (5/44)	100.0% (5/5)
S3	20.8% (10/48)	10.0% (1/10)	100.0% (1/1)	83.3% (40/48)	0% (0/40)	N/A
S4	13.3% (4/30)	75.0% (3/4)	0% (0/3)	66.7% (20/30)	25.0% (5/20)	100.0% (5/5)
S5	22.2% (8/36)	25.0% (2/8)	50.0% (1/2)	75.0% (27/36)	66.7% (18/27)	100.0% (18/18)
S6	0% (0/17)	N/A	N/A	94.1% (16/17)	25.0% (4/16)	25.0% (1/4)
S7	15.4% (2/13)	50.0% (1/2)	0% (0/1)	100% (13/13)	46.2% (6/13)	83.3% (5/6)
S8	16.7% (4/24)	25.0% (1/4)	100% (1/1)	100% (24/24)	25.0% (6/24)	83.3% (5/6)
S9	56.3% (9/16)	33.3% (3/9)	33.3% (1/3)	62.5% (10/16)	20.0% (2/10)	0% (0/2)
S10	18.4% (16/87)	18.8% (3/16)	66.7% (2/3)	100% (87/87)	21.8% (19/87)	94.7% (18/19)
S11	45.8% (11/24)	9.1% (1/11)	0% (0/1)	100% (24/24)	12.5% (3/24)	66.7% (2/3)
S12	14.3% (2/14)	0% (0/2)	N/A	64.3% (9/14)	11.1% (1/9)	100% (1/1)
S13	23.3% (7/30)	57.1% (4/7)	100% (4/4)	80.0% (24/30)	57.1% (4/24)	50.0% (2/4)
S14	38.9% (7/18)	0% (0/7)	N/A	94.4% (17/18)	23.5% (4/17)	100% (4/4)
S15	0% (0/21)	N/A	N/A	52.4% (11/21)	0% (0/11)	N/A
S16	66.7% (10/15)	30.0% (3/10)	66.7% (2/3)	86.7% (13/15)	7.7% (1/13)	0% (0/1)
S17	50.0% (3/6)	33.3% (1/3)	100% (1/1)	100% (6/6)	66.6% (2/6)	0% (0/2)

Supplementary Table 3. Cortical ripple coupling with hippocampal ripples for individual patients. *Significant Modulation:* Proportion of channel pairs with a significant increase in the conditional probability of a hippocampal ripple occurring in the first channel given that a cortical ripple occurred within ±500 ms in the second (one-sided randomization test, 200 shuffles, 25 ms non-overlapping bins, 3 consecutive bins each with post-FDR $p<0.05$ required for significance). *Significant Sidedness:* Those with significant modulations that had significant sidedness preference around $t=0$ (post-FDR $p<0.05$, two-sided binomial test, expected=0.5, -500 to -1 ms vs. 1 to 500 ms). *Cortical Ripple Leading:* Those with significant sidedness around 0 that had cortical ripples leading (according to counts within -500 to -1 ms vs. 1 to 500 ms). See Table 1 for aggregate results. N/A=not applicable since there were 0 channel pairs to be evaluated.

Patient	% Significant	
	NREM	Waking
S1	9.7%	65.3%
S2	58.5%	60.6%
S3	12.3%	6.8%
S4	1.5%	0.4%
S5	1.1%	17.9%
S6	19.7%	46.5%
S7	4.9%	40.2%
S8	1.8%	96.8%
S9	23.4%	4.5%
S10	7.6%	80.0%
S11	0%	66.1%
S12	17.3%	5.2%
S13	5.9%	50.8%
S14	29.8%	74.3%
S15	17.4%	17.8%
S16	29.5%	22.2%
S17	0%	4.8%
Average	14.1±15.2%	38.8±31.2%

Supplementary Table 4. Percent of channel-triplets where the number of triple co-occurrences significantly exceeded those that would be expected given the number of double co-occurrences of the constituent channel pairs. To test if the co-rippling between two particular cortical sites made it more likely that other cortical sites participated, we computed a χ^2 test of proportions for all possible groups of three cortical channels under the null hypothesis that the co-occurrence of channels A and B had no relation to the co-occurrence of A and C. *P*-values were FDR-corrected across channels for each patient. Error is standard deviation.

Patient	Immediate Recall		Delayed Recall	
	Accuracy	Time to Recall (s)	Accuracy	Time to Recall (s)
S18	150/150	1.18±0.14	139/150	1.47±0.45
S19	157/160	1.35±0.13	66/160	1.82±0.66
S20	86/104	0.95±0.15	33/104	2.57±0.60
S21	158/160	1.07±0.23	103/160	1.76±0.66
S22	147/160	1.10±0.21	24/160	2.19±0.73

Supplementary Table 5. Paired-associates memory task performance for individual patients. Values indicate successful recall counts divided by total recall cues and average time from recall cue presentation to successful recall onset. Word pair recall was considered successful when the second word was correctly stated aloud following the visual and auditory presentation of the first word. Immediate recall was assessed immediately following the presentation of the word pair to be learned and delayed recall was after ~60 s.

Channel pair type	No. Channel Pairs	State	>40 Co-occurring Ripples	Signif. PLV / Co-occurring	Signif. PLV / All Pairs
Cort ↔ Cort	2275	NREM	2106	26.3% (554/2106)	24.4% (554/2275)
		Waking	1939	13.9% (269/1939)	11.8% (269/2275)
Hipp ↔ Cort	461	NREM	277	1.4% (4/277)	0.9% (4/461)
		Waking	333	0.3% (1/333)	0.2% (1/461)

Supplementary Table 6. Significant cortico-cortical and hippocampo-cortical co-ripple PLVs. Channel pairs that had ≥40 co-occurring ripples with ≥25 ms overlap were used to compute the PLVs and test for significant modulations. Signif. PLV / co-occurring reports the percent of the channels with ≥40 co-occurring ripples that had significant PLV modulations. Sig. PLV / all pairs reports the percent of all channels (no minimum co-occurrence requirement) that had significant PLVs. Results are for patients S1-17. *P*-values were computed using a randomization test (200 shuffles/channel pair, 5 ms bins within ±50 ms relative to co-ripple temporal centers), and were FDR-corrected for multiple bins and channel pairs, and at least 2 consecutive bins with post-FDR $p<0.05$ were required for a pair to be significant.

Utah Array Patient Demographics							
Patient	Age	Sex	Handedness	Array Implantation Location		Probe Length (mm)	NREM Duration (min)
U1	51	F	R	Left middle temporal gyrus		1.0	200
U2	31	M	L	Left superior temporal gyrus		1.5	132
U3	47	M	R	Right middle temporal gyrus		1.5	120
Single Unit Characteristics							
Unit Type	No. Units	No. Spikes	Valley-to-Peak Amplitude (μV)	Spike Rate (Hz)	Valley-to-Peak Width (ms)	Half-Peak Width (ms)	Bursting Index
PY	142	318386	89.57±59.46	0.19±0.17	0.49±0.06	0.61±0.04	0.05±0.03
IN	38	772769	42.26±26.11	1.73±1.72	0.30±0.05	0.35±0.05	0.01±0.02

Supplementary Table 7. Single unit characteristics and patient demographics. Errors are standard deviations. IN=putative interneuron unit, PY=putative pyramidal unit.

References

1. E. Fernández *et al.*, Acute human brain responses to intracortical microelectrode arrays: challenges and future prospects. *Frontiers in Neuroengineering* **7** (2014).
2. C. J. Keller *et al.*, Heterogeneous neuronal firing patterns during interictal epileptiform discharges in the human cortex. *Brain* **133**, 1668-1681 (2010).
3. A. Waziri *et al.*, Initial surgical experience with a dense cortical microarray in epileptic patients undergoing craniotomy for subdural electrode implantation. *Neurosurgery* **64**, 540-545; discussion 545 (2009).
4. R. Oostenveld, P. Fries, E. Maris, J. M. Schoffelen, FieldTrip: Open source software for advanced analysis of MEG, EEG, and invasive electrophysiological data. *Comput Intell Neurosci* **2011**, 156869 (2011).
5. R. A. Mak-McCully *et al.*, Distribution, amplitude, incidence, co-occurrence, and propagation of human K-complexes in focal transcortical recordings. *eNeuro* **2** (2015).
6. R. Csercsa *et al.*, Laminar analysis of slow wave activity in humans. *Brain* **133**, 2814-2829 (2010).
7. B. Fischl, FreeSurfer. *NeuroImage* **62**, 774-781 (2012).
8. B. Fischl *et al.*, Automatically parcellating the human cerebral cortex. *Cereb Cortex* **14**, 11-22 (2004).
9. C. Destrieux, B. Fischl, A. Dale, E. Halgren, Automatic parcellation of human cortical gyri and sulci using standard anatomical nomenclature. *NeuroImage* **53**, 1-15 (2010).
10. J. E. Iglesias *et al.*, A computational atlas of the hippocampal formation using ex vivo, ultra-high resolution MRI: Application to adaptive segmentation of in vivo MRI. *NeuroImage* **115**, 117-137 (2015).
11. H. Johnson, G. Harris, K. Williams, BRAINSFit: mutual information rigid registrations of whole-brain 3D images, using the insight toolkit. *Insight J* 10.54294/hmb052 (2007).
12. A. Fedorov *et al.*, 3D Slicer as an image computing platform for the Quantitative Imaging Network. *Magn Reson Imaging* **30**, 1323-1341 (2012).
13. B. Fischl, M. I. Sereno, R. B. Tootell, A. M. Dale, High-resolution intersubject averaging and a coordinate system for the cortical surface. *Hum Brain Mapp* **8**, 272-284 (1999).
14. M. F. Glasser *et al.*, A multi-modal parcellation of human cerebral cortex. *Nature* (2016).
15. T. E. J. Behrens, H. J. Berg, S. Jbabdi, M. F. S. Rushworth, M. W. Woolrich, Probabilistic diffusion tractography with multiple fibre orientations: What can we gain? *NeuroImage* **34**, 144-155 (2007).
16. B. Q. Rosen, E. Halgren, A whole-cortex probabilistic diffusion tractography connectome. *eNeuro* 10.1523/ENEURO.0416-20.2020 (2021).
17. D. J. Hagler, Jr. *et al.*, Heterogeneous origins of human sleep spindles in different cortical layers. *J Neurosci* **38**, 3013-3025 (2018).
18. C. E. Gonzalez *et al.*, Theta bursts precede, and spindles follow, cortical and thalamic downstates in human NREM sleep. *J Neurosci* **38**, 9989-10001 (2018).
19. X. Jiang, J. Gonzalez-Martinez, E. Halgren, Coordination of human hippocampal sharpwave ripples during NREM sleep with cortical theta bursts, spindles, downstates, and upstates. *J Neurosci* **39**, 8744-8761 (2019).
20. X. Jiang, J. Gonzalez-Martinez, E. Halgren, Posterior hippocampal spindle-ripples co-occur with neocortical theta-bursts and down-upstates, and phase-lock with parietal spindles during NREM sleep in humans. *J Neurosci*, 2858-2818 (2019).
21. A. Delorme, S. Makeig, EEGLAB: An open source toolbox for analysis of single-trial EEG dynamics including independent component analysis. *J Neurosci Methods* **134**, 9-21 (2004).
22. P. Berens, CircStat: a MATLAB toolbox for circular statistics. *J Stat Softw* **31**, 1-21 (2009).

23. C. W. Dickey *et al.*, Travelling spindles create necessary conditions for spike-timing-dependent plasticity in humans. *Nature Communications* **12**, 1027 (2021).
24. J.-B. Eichenlaub *et al.*, Replay of learned neural firing sequences during rest in human motor cortex. *Cell Reports* **31**, 107581 (2020).
25. B. Teleńczuk *et al.*, Local field potentials primarily reflect inhibitory neuron activity in human and monkey cortex. *Scientific Reports* **7**, 40211 (2017).
26. M. Le Van Quyen *et al.*, High-frequency oscillations in human and monkey neocortex during the wake–sleep cycle. *Proceedings of the National Academy of Sciences* **113**, 9363-9368 (2016).
27. N. Dehghani *et al.*, Dynamic balance of excitation and inhibition in human and monkey neocortex. *Scientific Reports* **6** (2016).
28. A. M. Chan *et al.*, Speech-specific tuning of neurons in human superior temporal gyrus. *Cereb Cortex* **24**, 2679-2693 (2014).
29. A. Peyrache *et al.*, Spatiotemporal dynamics of neocortical excitation and inhibition during human sleep. *Proceedings of the National Academy of Sciences* **109**, 1731-1736 (2012).
30. J. Kamiński, A. Brzezicka, A. N. Mamelak, U. Rutishauser, Combined phase-rate coding by persistently active neurons as a mechanism for maintaining multiple items in working memory in humans. *Neuron* **106**, 256-264.e253 (2020).
31. C. Pouzat, O. Mazor, G. Laurent, Using noise signature to optimize spike-sorting and to assess neuronal classification quality. *J Neurosci Methods* **122**, 43-57 (2002).
32. S. Ray, Challenges in the quantification and interpretation of spike-LFP relationships. *Curr Opin Neurobiol* **31**, 111-118 (2015).
33. B. Pesaran, J. S. Pezaris, M. Sahani, P. P. Mitra, R. A. Andersen, Temporal structure in neuronal activity during working memory in macaque parietal cortex. *Nature Neuroscience* **5**, 805-811 (2002).
34. Y. Benjamini, Y. Hochberg, Controlling the false discovery rate: a practical and powerful approach to multiple testing. *Journal of the Royal Statistical Society. Series B (Methodological)* **57**, 289-300 (1995).
35. X. Jiang *et al.*, Improved identification and differentiation from epileptiform activity of human hippocampal sharp wave ripples during NREM sleep. *Hippocampus* (2019).